Synthesis of nanometer-sized gallium oxide using graphene oxide template as a photocatalyst for carbon dioxide reduction

Kenta Sonoda, Muneaki Yamamoto, Tetsuo Tanabe, Tomoko Yoshida

Synthesis of nanometer-sized gallium oxide using graphene oxide template as a photocatalyst for carbon dioxide reduction

Kenta Sonoda[1*], Muneaki Yamamoto[2*], Tetsuo Tanabe[2], Tomoko Yoshida[2]

[1] *Applied Chemistry and Bioengineering, Graduate School of Engineering, Osaka City University, Osaka 558-8585, Japan*

[2] *Research Center for Artificial Photosynthesis, Osaka City University, Osaka 558-8585, Japan*

*Corresponding author;
Phone number: +81-666053619
E-mail: m19tc024@hg.osaka-cu.ac.jp (Kenta Sonoda)
m-yamamoto@osaka-cu.ac.jp (Muneaki Yamamoto)

Abstract

Since the activity of semiconductor photocatalysts on CO_2 reduction with water is still low, it is necessary to improve their activity with controlling their particle sizes and crystal structures. In previous studies, we have reported that micro-particulate Ga_2O_3 deposited on Al_2O_3 support significantly improves the photocatalytic activity of CO_2 reduction. However, it is quite difficult to synthesize nano-particulate Ga_2O_3 with high crystallinity by calcination at higher temperatures. In this work, we have tried to synthesize sheet-like nano-particulate Ga_2O_3 using graphene oxide (GO) as a template for the first time. After loading gallium butoxide on GO, it was calcined to oxidize the gallium butoxide into Ga_2O_3 and also to remove GO. Various spectroscopic analyses revealed that the synthesized materials were planar aggregation of nanometer-sized Ga_2O_3 particles (nsGa_2O_3), of which sizes and crystallinity could be controlled with the calcination temperature. The nsGa_2O_3 calcined at 1123 K was well crystallized and showed β-phase with a quite large specific surface area. Furthermore, Ag loaded nsGa_2O_3 calcined at 1123 K (Ag/nsGa_2O_3(1123 K)) showed very high photocatalytic activity for CO production in the photocatalytic CO_2 reduction test in aqueous solution including methanol under UV light irradiation. Thus, it is confirmed that the planar aggregation of nanometer-sized Ga_2O_3 significantly improves the photocatalytic activity of Ga_2O_3 on the CO_2 reduction.

Keywords: CO_2 reduction; photocatalyst; nano-particulate Ga_2O_3; graphene oxide

Introduction

Photocatalytic reduction of CO_2 with water using a metal oxide photocatalyst has been attracting much attention for mitigation of environmental problems [1-4], and various oxides have been developed as the photocatalyst. Among all, Ga_2O_3 is one of the most attractive photocatalysts for both CO_2 reduction [5, 6] and water splitting [7-9]. It is also well known that Ag loading on Ga_2O_3 as a co-catalyst enhances its photocatalytic activity on the CO_2 reduction as well as the water splitting [10-13].

In previous works, it is shown that fine particles of Ga_2O_3 exhibiting mixed phases of γ- and β-, or defective β-phase show high photocatalytic activity on the CO_2 reduction with water under UV light irradiation [5, 6]. Ito *et al.* have reported that homogeneous loading of micro-particulate Ga_2O_3 on Al_2O_3 significantly improves the photocatalytic activity of CO_2 reduction [14]. In these respects, nano-particulate Ga_2O_3 which is basically defective owing to their large surface to volume ratio would be a better photocatalyst. However, the nanoparticulates easily become three dimensional aggregate with larger sizes and difficult to be dispersed separately in water. In this respect, ultrathin two-dimensional (2D) structure, i.e. nano-sheets would be suitable as a photocatalyst, because of their unique properties different from bulk, such as, most of atoms being on the surface, very short distance of charge carriers, efficient photon acceptance and so on. Quite recently, Zhang *et al.* [15] have synthesized two-dimensional β-Ga_2O_3 nano-sheets from ultrathin γ-Ga_2O_3 nano-sheets. However, it seems hard to control crystalline phases among α, β and γ as well as their sizes. Takenaka *et al.* have succeeded to

synthesize polycrystalline metal oxide nanosheet with using graphene oxide (referred as GO hereafter) as a template.

In this work, we have applied GO as a template to synthesize sheet-like nanometer-sized particulate Ga_2O_3 (denoted as nsGa_2O_3) using graphene oxide first time and tried to control crystalline phases of nanoparticulates and their sizes with changing calcination temperature. After loading very thin gallium butoxide on the GO surface, it was calcined at higher temperatures to remove GO and obtain planar aggregates of crystallized nsGa_2O_3. Since the synthesis of nsGa_2O_3 applying the GO template is the first time, as far as we know, products appeared in each stage during the synthesis were examined in detail with various techniques to characterize their morphologies, structures and surface states. Depending on the calcination temperature, the crystalline phase of resultant nsGa_2O_3 was changed. Using synthesized nsGa_2O_3 consisting of β-phase only as a catalyst with Ag loading, a photocatalytic CO_2 reduction test was conducted. The result was compared with that obtained using commercially available β-Ga_2O_3 (β-Ga_2O_3) as the photocatalyst. In the tests, we have added methanol which stabilized the loading state of the Ag cocatalyst as nm sized particles and gave reproducible results [16]. It was confirmed that the addition of methanol hardly influenced the photocatalytic CO_2 reduction [16, 17]. This makes the comparison of the photocatalytic activities of nsGa_2O_3 and bulk β-Ga_2O_3 meaningful.

Experimental

Sample preparation method:

Figure 1 schematically shows synthesis processes, in which the results of characterizations given in the following sections were included. 500 mg of dried GO which was obtained by the exfoliation of the graphitic oxide [18, 19] following the Hummer's method [20] and 1.53 g of $Ga(OnC_4H_9)_3$ (referred to as $Ga(OBu)_3$) were suspended in 500 mL of cyclohexane (super dehydrated, Wako Pure Chemicals). The suspension was stirred at room temperature (RT) for several days in order to disperse dried GO in cyclohexane homogeneously and to load $Ga(OBu)_3$ on the dried GO. Above processes were carried out in a nitrogen purged glove box because $Ga(OBu)_3$ is highly deliquescent. The obtained material is denoted as $Ga(OBu)_3$/GO. $Ga(OBu)_3$/GO was dispersed in 540 mL of cyclohexane and transferred to Teflon containers in a stainless-steel autoclave. Then the autoclave was heated at 453 K for 6 h. During the heating, $Ga(OBu)_3$ was mostly oxidized to be GaO_x and GO was partly reduced and referred to as rGO. Then, the resultant material was centrifuged and dried in a vacuum overnight to get GaO_x/rGO. Finally, GaO_x/rGO was calcined in air at a temperature ranging from 823 to 1123 K for 2 h (temperature raising rate: 2 °C/min) to get sheet-like nsGa_2O_3 (denoted as nsGa_2O_3(X K), where X indicates the calcination temperature).

Silver loading method:

Photocatalytic CO_2 reduction tests were conducted using nsGa_2O_3 with Ag loading as a co-catalyst. Commercially available β-Ga_2O_3 (Kojundo Chemical Laboratory Co., Ltd., Purity 99.99%, denoted as β-Ga_2O_3) was also tested for the comparison. The 0.5 wt% Ag co-catalyst was loaded by a photodeposition method with using $AgNO_3$ (Kishida Chemical Co., Ltd., Purity 99.8%) as a precursor. However, the loaded Ag co-catalyst on nsGa_2O_3 was unstable in water under UV light irradiation to be oxidized or reduced to large metallic particles, resulting in the loss of catalytic activity. Recently we have succeeded to control and stabilize the size and distribution of Ag nanoparticles (Ag NPs) on Ga_2O_3 photocatalysts with using aqueous solution of methanol [16]. Therefore, the photocatalytic CO_2 reduction tests were conducted using the aqueous solution of methanol with the optimized concentration of 17 vol%, which made Ag-NPs stable during the photocatalytic CO_2 reduction tests and gave reproducible results to compare the photocatalytic activities of synthesized nsGa_2O_3 with that of β-Ga_2O_3.

Photocatalytic CO_2 reduction test:

Three samples were subjected to photocatalytic CO_2 reduction tests; two samples consisting of the β phase (nsGa_2O_3 (1023 K) and ns Ga_2O_3 (1123 K)), and β-Ga_2O_3 with Ag loaded as a co-catalyst. The loaded amounts were determined as 0.24, 0.39 and 0.33 wt%, respectively from X-ray fluorescence

spectroscopy measurement. Three samples are referred to as Ag/nsGa_2O_3(1023 K), Ag/nsGa_2O_3(1123 K) and Ag/β-Ga_2O_3) hereafter.

The photocatalytic CO_2 reduction tests were carried out in a fixed-bed flow reactor cell. 50 mg of the sample was dispersed in the aqueous solution of 10 mL of $NaHCO_3$ (1 M) and 2 mL of methanol. The air in the cell was replaced with CO_2 gas with the flow rate of 50 mL/min for 30 min. Then, the tests were conducted with UV irradiation under the CO_2 gas with the flow rate of 3.0 mL/min. A 300 W Xe lamp was used as the UV source and its light intensity was about 25 mW/cm^2 in the wavelength range of 254 ± 10 nm. The reaction products (mainly CO and H_2) were analyzed by a gas chromatograph equipped with a thermal conductivity detector. Without the CO_2 flow in the reaction cell, the amount of produced CO was very small. This confirms that methanol hardly influenced the CO_2 reduction in the present experiments as already found in previous works [16, 17].

Characterization of the Samples:

For understanding of the formation process of nsGa_2O_3, thermogravimetric analysis (TGA) was conducted with a Thermo plus EVO2 (Rigaku) using a Pt pan sample holder in air, with a heating rate of 5 K/min. Characterization of samples was performed by a transmission electron microscope (TEM), a scanning electron microscope (SEM), X-ray diffraction (XRD), X-ray absorption fine structure (XAFS) and UV−Vis diffuse reflectance (UV-Vis DR). Specific surface area (SSA) was also measured.

TEM images of the samples were acquired with JEM-2100F, operating at 200 kV. SEM images of the samples were acquired with JSM-6500F, operating at 15 kV. XRD patterns of the samples were recorded on a MiniFlex600 (Rigaku) using Cu Kα as a radiation source with an operating voltage of 40 kV and current of 15 mA. The XRD patterns were collected at 2θ angles of 10 − 80°. The 2θ step size was 0.02°, and the scanning rate was 5°/min. Ga K-edge XAFS spectra of nsGa_2O_3 were measured at the beamline 5S1 in Aichi Synchrotron Radiation Center using a Si(111) double-crystal monochromator at RT. The data were recorded in a transmission mode. Ga L_3-edge XAFS spectra were recorded in a fluorescence yield mode at beamline 2A in UVSOR, Institute for Molecular Science, using beryl double-crystal monochromator at RT. SSA of the samples were determined by Brunauer-Emmett-Teller (BET) SSA measurements at 77 K (liquid N_2 temperature) using Monosorb (Quantachrome). Before the BET measurements, the samples were heated at 573 K for 3 h in N_2 atmosphere as a pretreatment. The adsorbed amounts of CO_2 on nsGa_2O_3 samples and their chemical states were investigated by in-situ FT-IR measurements using FT/IR-6100 (JASCO) in the transmission mode at RT. The sample (ca. 15 mg) was pressed into a disk (diameter: 10 mm) at 50 MPa and placed in an in-situ IR cell equipped with CaF_2 window. The cell allowed us in-situ measurements as well as sample heating, introduction of the reactant gas and UV light irradiation. Before the in-situ measurement, the sample was pretreated with evacuation at RT for 3 h. UV-Vis DR spectra were measured at RT using a spectrometer (JASCO V-670). The spectrum of Ba_2SO_4 was used as the reference. The concentration of loaded Ag on Ga_2O_3 was determined by X-ray fluorescence (XRF) measurement using with EDX-720 (Shimadzu) whose primary X-ray source is Rh.

Results:

Process of sheet-like nanometer-sized particulate Ga_2O_3 (nsGa_2O_3) formation

As mentioned in the experimental section, GO was partly reduced and GaO_x/rGO was produced during the heat treatment at 453 K in the autoclave. The following calcination of GaO_x/rGO at higher temperature resulted in the planar aggregates of nsGa_2O_3 by removing rGO and full oxidation of GaO_x. In order to understand the above process, TGA analysis was done both for GO and GaO_x/rGO in the temperatures ranging from 300 to 900 K. The results were given in Fig. 2. The weight losses of GO appeared at around 320 K and 500 K were caused by water desorption and oxidative evaporation of functional groups such as -OH and -COOH in GO, respectively [20]. The full combustion of carbon started at around 800 K and completed at 900 K. In the TGA profile of GaOx/rGO, the gradual loss continued until the final full combustion. Since no clear loss corresponding to the evaporation of the functional groups was observed, GO must be mildly reduced during the autoclave treatment. That is the reason for using the terminology of rGO. The oxidation of GaOx could have positive weight gain to compensate the weight loss by the evaporation. After the full combustion at around 900 K only

Ga_2O_3 remained. From the weight of the remained Ga_2O_3, we have determined the loading amount of Ga_2O_3 in the GaO_x/rGO to be 25 wt% which included some uncertainty caused by the full oxidation of GaOx to Ga_2O_3.

Figure 3 shows SEM images of GaO_x/rGO, and Figure 4 shows TEM images of GO and GaO_x/rGO. The SEM images clearly show that GaO_x/rGO is consisting of petal-like sheets with their width of around a few μm. Each sheet of GaO_x/rGO is transparent in the TEM image. The sheet seems homogenous and a little thicker than GO sheet except some segregation of GaO_x which is appreciable as local black colored areas. The existence of GaO_x on rGO was confirmed by the appearance of amorphous like patterns in XRD (See Fig. 7(a)). In EXAFS analysis, the existence of GaO_x was also confirmed, and the bonding or coordination of a gallium atom to the first and second neighboring ones were depicted as described below.

Here Fig.1 is indicated how nsGa_2O_3 synthesis proceeded according to the obtained results.

Characterization of GaO_x/rGO

Figure 5 (a, b) shows k^3-weighted Ga K-edge EXAFS spectra of GaO_x/rGO together with that of β-Ga_2O_3. The oscillation intensity of the EXAFS spectrum of GaO_x/rGO was high at the low wavenumber around k=4 $Å^{-1}$. This indicates that light atoms such as C and O were coordinated to a Ga atom. As for β-Ga_2O_3, another high intensity of the EXAFS oscillation appeared at the wavenumber around k=9 $Å^{-1}$, which suggests additional coordination between heavy Ga atoms.

Figures 5c and d show radial structure functions (RSFs) obtained by Fourier transform of the Ga K-edge EXAFS of GaO_x/rGO and β-Ga_2O_3 (Figure 5 (a, b)), respectively. As for RSFs, the first peak around 1-2 Å was assigned to the backscattering from an adjacent atom to a gallium atom, corresponding to Ga-O bond for both β-Ga_2O_3 and GaO_x/rGO. Although the second peak around 2.5-3 Å appeared in the RSF of GaO_x/rGO (Fig. 5(c)) seems well corresponding to the second-neighboring Ga atoms (Ga-(O)-Ga) appeared in the RSF of β-Ga_2O_3 (Fig. 5(d)) [22-24], the curve-fitting analysis of GaO_x/rGO suggests that the second peak is caused by Ga-O and Ga-C bonds having longer interatomic distances than first neighboring Ga-O bond. The appearance of these longer Ga-O and Ga-C bonds is likely caused by the junction between GaO_x species and rGO in atomic scales. The absence of Ga-(O)-Ga bond also suggests GaO_x species on rGO were highly dispersed rather than aggregated.

Characterization of nsGa_2O_3

Figure 6 compares TEM images of nsGa_2O_3(823 -1123 K) and β-Ga_2O_3. The images clearly indicate the difference in the morphology among synthesized nsGa_2O_3 and β-Ga_2O_3. It should be noted that two dimensional structure of the GaO_x/rGO was maintained after the removal of the rGO. Thus, sheet-like materials consisting of nano-sized polycrystalline were successfully synthesized by the present method. Although the average size of polycrystalline became larger with increasing the calcination temperature, planar aggregate structures made of nano-particulates were maintained even for nsGa_2O_3 calcined at such high temperature as 1123 K (sample nsGa_2O_3(1123K)).

Table 1 shows the results of BET SSA measurements for nsGa_2O_3(823 - 1123 K) and β-Ga_2O_3. It should be noted that SSA of nsGa_2O_3 (823 - 1123 K) are larger than that of β-Ga_2O_3 about 18, 11, 9.8 and 6.5 times, respectively.

In Figure 7, XRD patterns of GaO_x/rGO, nsGa_2O_3(823 - 1123 K) and β-Ga_2O_3 were compared. The XRD pattern of GaO_x/rGO spreads widely with low intensity, including a broad peak assigned to (002) plane of graphite (Figure 7 (a)) [25]. This indicates that very thin amorphous like GaO_x or highly dispersed small GaO_x particles were loaded on rGO. As the calcination temperature increased, the crystallinity of nsGa_2O_3 samples was improved. The higher the crystallinity of nsGa_2O_3 became, the smaller SSA was. The XRD patterns of nsGa_2O_3(823, 923 K) were consisting of the mixed diffraction patterns of β-Ga_2O_3 and γ-Ga_2O_3, while those of nsGa_2O_3(1023, 1123 K) were assigned to the single phase of β-Ga_2O_3. Thus, after removing rGO from GaO_x/rGO by calcination, GaO_x turned to be aggregation of nano-sized particles, which maintained the sheet like form and consisted of mixed phases of γ and β by calcination at 823-923 K. The calcination above 1023 K made all particles to the single phase of β-Ga_2O_3.

The crystallite size was calculated from the full width at half maximum (FWHM) of the most intense diffraction peak using the Scherrer's equation as shown in Table 1. Since the crystallite sizes derived

from the Scherrer's equation was consistent with that observed in the TEM images in Figure 6 (b), (d), (f) and (h), it can be concluded that nsGa_2O_3 were formed by crystallization of amorphous like Ga_2O_3 sheet and aggregation of the crystallized nano-particles with keeping the sheet like form.

Figure 8 compares Ga L_3-edge XANES spectra of single phases of α, β and γ in (a) with those of nsGa_2O_3 in (b). It is known that Ga L_3-edge XAFS analysis gives more detailed information on the local symmetry structures of nsGa_2O_3 compared with Ga K-edge XAFS analysis. As seen in Figure 8 (a), the intensities of the peak around 1107 eV decreases in the order of α-Ga_2O_3, γ-Ga_2O_3 and β-Ga_2O_3. The main difference among these three phases is number density of hexacoordinated Ga atoms structure; the highest one is α-Ga_2O_3 in which all Ga atoms are hexacoordinated, the second, γ-Ga_2O_3 including some tetracoordinated Ga atoms, and the least, β-Ga_2O_3 consisting of hexacoordinated Ga and tetracoordinated Ga atoms evenly.

As shown in Fig. 8(b), the peak intensity around 1107 eV of the Ga L_3-edge XANES spectra of nsGa_2O_3 decreased with increasing the calcination temperature. This indicates that nsGa_2O_3 calcined at lower temperature were mainly composed of hexacoordinated Ga atoms, while the calcination of nsGa_2O_3 at higher temperature increases tetracoordinated Ga atmos. This is consistent with the results of XRD measurement.

Although Ga K-edge EXAFS spectra of nsGa_2O_3(1123 K) and β-Ga_2O_3 were similar with each other (Figure 9(a)), derived RSFs from them showed the important difference; the second peak at around 2.7 Å attributed to Ga-(O)-Ga bond was lower for nsGa_2O_3(1123 K) than that of β-Ga_2O_3 (See Figure 9(b)). Using the curve fitting, the coordination number for Ga-(O)-Ga bond was evaluated and given in Table 2. The coordination number in nsGa_2O_3 is a little smaller than that in β-Ga_2O_3. Considering that EXAFS provides sub-nm or nm sized local structure, the difference in the coordination number suggests that nsGa_2O_3(1123 K) consisting of β-Ga_2O_3 crystalline structure is a little defective compared to fully crystalized one, owing to its very thin planer structure consisting of nano-particulate.

Photocatalytic CO_2 reduction

Figure 10 compares the production rates of H_2 and CO and the selectivity toward CO evolution observed for three tested samples in photocatalytic CO_2 reduction tests using aqueous solution with methanol. H_2 and CO were continuously evolved throughout the reaction tests for both samples. CO production rate of Ag/nsGa_2O_3(1123 K) was over 2 times higher than that of Ag/β-Ga_2O_3, while H_2 production rate was lower. Consequently, CO selectivity (the ratio of CO production amount to total amounts of reduction products) of Ag/nsGa_2O_3(1123 K) reached 70 %. nsGa_2O_3 (1023 K) showed a little less activity than that for nsGa_2O_3 (1123 K), probably because its crystallinity was less than that of the latter. Hence the discussion was focused to comparison of Ag/nsGa_2O_3(1123 K) and Ag/β-Ga_2O_3.

Since CO could be evolved from methanol or $NaHCO_3$, the reduction test without CO_2 flow was conducted. As shown in Figure 11, the CO production rate without CO_2 flow was only 1.5-3.4 μmol/h. Furthermore, no CO production was observed without Ag/nsGa_2O_3. Therefore, it is confirmed that most of the generated CO was derived from the photocatalytic CO_2 reduction and nsGa_2O_3 prepared by the present method was suitable for CO_2 reduction rather than H_2 production from water compared to β-Ga_2O_3 used here.

Discussion

It was found that nsGa_2O_3 (sheet-like nanometer-sized particulate Ga_2O_3) exhibiting well crystallized β-phase gave better performance in photocatalytic CO_2 reduction than that given by β-Ga_2O_3. The improvement is, in some sense, a corollary of ultrafine particulation, as appeared in the increase of SSA. Still nsGa_2O_3 exhibits different characters relating photocatalytic activity compared with those of β-Ga_2O_3. They are CO_2 absorption capability and states of Ag cocatalyst on them.

To reveal the adsorbed species on nsGa_2O_3 and β-Ga_2O_3 as prepared, in-situ FT-IR measurements were conducted. Figure 12 shows FT-IR spectra in wavelength range 2600-3800 cm^{-1}, which represent adsorbed water or hydroxyl groups on nsGa_2O_3(1123 K) and β-Ga_2O_3. The larger peak intensity for nsGa_2O_3(1123 K) than β-Ga_2O_3 well corresponds to the larger SSA of the former. Since nsGa_2O_3(1123 K) exhibiting β-Ga_2O_3 phase was a little defective compared to fully crystalized one, included defects in nsGa_2O_3(1123 K) likely contribute to provide adsorption sites for hydroxyl groups. To make

detailed comparison on adsorbed hydroxyl groups on both samples, the two FT-IR spectra are compared by normalizing with their peak intensity at 3463 cm^{-1} as the inset of Fig. 12. Two peaks at 3720 and 3653 cm^{-1} are appreciable, which are assigned to the stretching vibration of single and bridge bonded hydroxyl groups, respectively [26]. The larger intensity of these peaks for nsGa_2O_3(1123 K) than β-Ga_2O_3 indicates that the former adsorbed more hydroxyl groups compared to the latter.

Figure 13 shows the difference FT-IR spectra of the adsorbed species on nsGa_2O_3(1123 K) and β-Ga_2O_3 after introduction of 45 Torr of CO_2. The absorption bands at 1635 and 1420 cm^{-1} are assigned to asymmetric CO_3 stretching vibration [$\nu_{as}(CO_3)$] and symmetric CO_3 stretching vibration [$\nu_s(CO_3)$] of monodentate bicarbonate species, respectively [27-30], while the bands at 1590 and 1320 cm^{-1} are attributed to $\nu_{as}(CO_3)$ and $\nu_s(CO_3)$ of bidentate carbonate species, respectively [27-29]. CO_2 molecules would react with the surface hydroxyl groups and the surface lattice oxygen of Ga_2O_3 to form the monodentate bicarbonate species and bidentate carbonate species [31, 32]. The former is assigned to be an intermediated state for CO production over Ga_2O_3 [33]. The significant increases of monodentate bicarbonate species on nsGa_2O_3(1123 K) compared to those on β-Ga_2O_3 could be one of the causes for the higher CO production on nsGa_2O_3(1123 K).

Figure 14 shows UV-Vis diffuse reflectance spectra of nsGa_2O_3(1123 K) and β-Ga_2O_3 with comparison of Ag/nsGa_2O_3(1123 K) and Ag/β-Ga_2O_3 after use for the photocatalytic CO_2 reduction test. Before the Ag loading, the absorption derived from the bandgap transition of Ga_2O_3 appeared at < 290 nm in both samples (Figure 14a). As for Ag/nsGa_2O_3(1123 K) and Ag/β-Ga_2O_3 after use (Figure 14b), an absorption peak around 430 nm attributed to localized surface plasmon resonance (LSPR) of small Ag nanoparticle (Ag NPs) was observed [32]. It should be mentioned that without methanol addition, Ag-NPs on nsGa_2O_3 were not stable and the absorption peak around 430 nm were broadened and/or decreased by accompanying the activity loss. Recently, we have found the nearly linear relationship of the LSPR intensity (i.e., the number density of small Ag NPs) and the CO production rate and concluded that Ag NPs showing the LSPR absorption peak are active sites for the CO_2 reduction [16]. Since the LSPR peaks were sharp and more intense in Ag/nsGa_2O_3(1123 K) than Ag/β-Ga_2O_3, Ag NPs should be densely deposited on nsGa_2O_3(1123 K) than on β-Ga_2O_3. Actually, TEM observations given in Fig 15 confirmed this, i.e. Ag NPs with the sizes of ca. 20 nm or less were loaded on both samples while the larger Ag NPs with the size of around 50 nm or more were also deposited for Ag/β-Ga_2O_3. The size distributions are given in Figure 16. Thus ultrafine particulation of Ga_2O_3 seems to stabilize AgNPs to be ca. 20 nm or less, the suitable size as Ag cocatalyst by avoiding their aggregation.

Conclusions

We have succeeded in synthesizing sheet-like Ga_2O_3 (nsGa_2O_3) with using GO as a template by loading Ga_2O_3 precursor on GO followed by GO removal by calcination at higher temperatures. The synthesized nsGa_2O_3 consists of the planner aggregation of the nanometer-sized Ga_2O_3 particles which are much smaller than those of Ga_2O_3 synthesized by a simple calcination such as commercially available β-Ga_2O_3 and other synthesized Ga_2O_3 samples in our previous work [5]. Accordingly, the specific surface area (SSA) of nsGa_2O_3(1123 K) was much larger than that of β-Ga_2O_3. The crystallinity and crystalline phase of nsGa_2O_3 were changed with the calcination temperature. Among all synthesized nsGa_2O_3 samples, nsGa_2O_3(1123 K) which was consisted of the only β-phase showed the highest CO production rate and CO selectivity in the photocatalytic CO_2 reduction with water including $NaHCO_3$ and methanol.

Thus, we can conclude that nsGa_2O_3 (sheet-like nanometer-sized particulate Ga_2O_3) exhibiting well crystalized β-phase gives better performance in photocatalytic CO_2 reduction. At the present stage, it is difficult to mention the particular cause for the improvement. Observed changes in characters relating the photocatalytic CO_2 reduction are the increase of SSA, larger CO_2 adsorption ability and the loading state of Ag co-catalyst. Those are in some sense a corollary of ultrafine particulation. Still the crystalline phase and crystallite size of nsGa_2O_3 were not fully controlled, it remains as a future work to optimize them for further improvement of the activity of nsGa_2O_3 for photocatalytic CO_2 reduction.

Acknowledgements

This work was supported continuously by Prof. Takenaka, Mr. Sugiyama and Mr. Suzuki of Doshisya University in the preparation of Ga_2O_3 nano-sheets. Synchrotron experiments were carried out at Aichi Synchrotron Radiation Center and UVSOR Institute for Molecular Science which are supported by No. 2503042 and 2019-510, respectively. This work was supported by Kansai Research Foundation for Technology Promotion.

References

[1] O. K. Varghese, M. Paulose, T. J. LaTempa, C. A. Grimes, Nano Lett. 9 (2009) 731−737.
[2] W. Tu, Y. Zhou, Z. Zou, Adv. Mater. 26 (2014) 4607−4626.
[3] K. Sekizawa, K. Maeda, K. Domen, K. Koike, O. Ishitani, J. Am. Chem. Soc. 135 (2013) 4596−4599.
[4] S. Sato, T. Morikawa, T. Kajino, O. Ishitani, Angew. Chem. Int. Ed. 52 (2013) 988−992.
[5] M. Akatsuka, Y. Kawaguchi, R. Ito, A. Ozawa, M. Yamamoto, T. Tanabe, T. Yoshida, Appl. Catal. B 262 (2019) 118247.
[6] Y. Kawaguchi, M. Yamamoto, A. Ozawa, Y. Kato, T. Yoshida, Surf. Interface Anal. 51 (2018) 1−6.
[7] H. H. Tippins, Phys. Rev. 140 (1965) 316−319.
[8] Y. Sakata, T. Hayashi, R. Yasunaga, N. Yanaga, H. Imamura, Chem. Commun. 51 (2015) 12935−12938.
[9] M. Passlack, E. F. Schubert, W. S. Hobson, M. Hong, N. Moriya, S. N. G. Chu, K. Konstadinidis, J. P. Mannaerts, M. L. Schnoes, G. J. Zydzik, J. Appl. Phys. 77 (1995) 686−693.
[10] K. Teramura, Z. Wang, S. Hosokawa, Y. Sakata, T. Tanaka, Chem. Eur. J. 20 (2014) 9906−9909.
[11] Z. Wang, K. Teramura, S. Hosokawa, T. Tanaka, J. Mater. Chem. A 3 (2015) 11313−11319.
[12] K. Teramura, T. Tanaka, Phys. Chem. Chem. Phys. 20 (2018) 20733.
[13] N. Yamamoto, T. Yoshida, S. Yagi, Z. Like, T. Mizutani, S. Ogawa, H. Nameki, H. Yoshida, e-J. Surf. Sci. Nanotech. 12 (2014) 263−268.
[14] R. Ito, M. Akatsuka, A. Ozawa, Y. Kato, Y. Kawaguchi, M. Yamamoto, T. Tanabe, T. Yoshida, ACS Omega 4 (2019) 5451−5428.
[15] X. Zhang, H. Huang, Y.Zhang, D. Liu, N. Tong, J. Lin, L. Chen, Z. Zhang, X. Wang, ACS Omega 3 (2018) 14469−14476.
[16] K. Yoshioka, M.Yamamoto, T. Tanabe, T. Yoshida, e-J. Surf. Sci. Nanotech. 18 (2020) 168−174.
[17] R. Ito, M. Akatsuka, A. Ozawa, M. Yamamoto, T. Tanabe, T. Yoshida, Bull. Chem. Soc. Japan 93 (2020) 694−700.
[18] I. Ogino, Y. Yokoyama, S. Iwamura, S. R. Mukai, Chem. Mater. 26 (2014) 3334−3339.
[19] S. Eigler, A. Hirsch, Angew. Chem. Int. Ed. 53 (2014) 7720−7738.
[20] W. S. Hummers, R. E. Offeman, J. Am. Chem. Soc. 80 (1958) 1339.
[21] S. Takenaka, S. Miyake, S. Uwai, H. Matsune, M. Kishida, J. Phys. Chem. C 119 (2015) 12445−12454.
[22] Y. Kato, M. Yamamoto, A. Ozawa, Y. Kawaguchi, A. Miyoshi, T. Oshima, K. Maeda, T. Yoshida, e-J. Surf. Sci. Nanotechnol. 16 (2018) 262−266.
[23] M. Akatsuka, T. Yoshida, N. Yamamoto, M. Yamamoto, S. Ogawa, S. Yagi, J. Phys. Conf. Ser. 712 (2016) 012056.
[24] K. Nishi, K. Shimizu, M. Takamatsu, H. Yoshida, A. Satsuma, T. Tanaka, S. Yoshida, T. Hattori, J. Phys. Chem. B 102 (1998) 10190−10195.
[25] Z. Q. Li, C. J. Lu, Z. P. Xia, Y. Zhou, Z. Luo, Carbon 45 (2007) 1686−1695.
[26] R. Pohle, M. Fleischer, H. Meixner, Sens. Actuators B Chem. 68 (2000) 151−156.
[27] S. E. Collins, M. A. Baltanas and A. L. Bonivardi, J. Phys. Chem. B 110 (2006) 5498−5507.
[28] S. E. Collins, M. A. Baltanas and A. L. Bonivardi, J. Catal. 226 (2004) 410−421.
[29] G. Busca and V. Lorenzelli, Mater. Chem. 7 (1982) 89−126.
[30] H. Tsuneoka, K. Teramura, T. Shishido and T. Tanaka, J. Phys. Chem. C 114 (2010) 8892−8898.
[31] M. Primet, P. Pichat and M.-V. Mathieu, J. Phys. Chem. 75 (1971) 1216−1220.
[32] S. Neatu, J. A. Macia-Agullo, P. Concepcion and H. Garcia, J. Am. Chem. Soc. 136 (2014) 15969−15976.

[33] M. Yamamoto, T. Yoshida, N. Yamamoto, T. Nomoto, Y. Yamamoto, S. Yagi, H. Yoshida, e-J. Surf. Sci. Nanotech. 12 (2014) 299−303.

Table 1. Specific surface area (SSA), crystalline size for β- or γ-phase of $nsGa_2O_3$ and β-Ga_2O_3.

Sample	Crystallite sizes determined by the Scherrer's equation		SSA(m^2/g)
	β-phase (nm)	γ-phase (nm)	
$nsGa_2O_3$(823K)	1.4	1.9	186
$nsGa_2O_3$(923K)	4.1	2.2	112
$nsGa_2O_3$(1023K)	9.2	-	98.1
$nsGa_2O_3$(1123K)	13.1	-	65.1
β-Ga_2O_3	33.3	-	10.2

Table 2. Characterization results of nsGa_2O_3(1123 K) and β-Ga_2O_3 :Curve fitting result of Ga K-edge EXAFS for second neighboring Ga atoms, specific surface area (SSA) and the Ag loading amount

Sample	SSA (m^2/g)	Ag loading (wt%)	Curve fitting results			
			N	R (Å)	dE (eV)	DW(Å)
nsGa_2O_3 (1123 K)	65.1	0.39	10.3	3.34	1.8	0.06
β- Ga_2O_3	10.2	0.33	11.0	3.34	0	0.06

N: coordination number, R: interatomic distance, dE: edge shift, DW: Debye Waller factor

Figure captions

Figure 1. The schematic drawing for synthesis process of GaO_x/rGO, $nsGa_2O_3$, Ag/$nsGa_2O_3$.

Figure 2. TGA profiles of GO and GaO_x/rGO measured in air.

Figure 3. SEM images of GaO_x/rGO (a) with an enlarged view (b).

Figure 4. TEM images of GO (a) and GaO_x/rGO (b). Note that both are transparent or semi-transparent in TEM. Holes are owing to sample holder.

Figure 5. Ga K-edge EXAFS spectra of GaO_x/rGO (a) and β-Ga_2O_3 (b), and corresponding radial structure functions derived by Fourier transform of the EXAFS spectra of GaO_x/rGO (c) and β-Ga_2O_3 (d).

Figure 6. TEM images of $nsGa_2O_3$(823 K) (a, b), $nsGa_2O_3$(923 K) (c, d), $nsGa_2O_3$(1023 K) (e, f), $nsGa_2O_3$(1123 K) (g, h) and β-Ga_2O_3 (i).

Figure 7. XRD patterns of GaO_x/rGO (a), $nsGa_2O_3$(823 K) (b), $nsGa_2O_3$(923 K) (c), $nsGa_2O_3$(1023 K) (d), $nsGa_2O_3$(1123 K) (e) and β-Ga_2O_3 (f).

Figure 8. XANES spectra of Ga_2O_3 of α, β, γ-Ga_2O_3 as reference samples (a) and $nsGa_2O_3$ (823 – 1123 K) (b).

Figure 9. k^3-weighted Ga K-edge EXAFS spectra of $nsGa_2O_3$ (1123 K) and β-Ga_2O_3 (a) and their radial structural functions obtained by Fourier transforming the EXAFS spectra (b).

Figure 10. Comparison of H_2 and CO production rates and selectivity toward CO evolution between Ag/$nsGa_2O_3$(1023, 1123 K) (a, b) and Ag/β-Ga_2O_3 (c) in the photocatalytic CO_2 reduction.

Figure 11. CO production rates in the photocatalytic reaction with He flow without CO_2 using $nsGa_2O_3$(1123 K).

Figure 12. FT-IR spectra representing adsorbed water or hydroxyl groups on $nsGa_2O_3$(1123 K) (black line) and β-Ga_2O_3 (grey line). The inset shows normalized ones with the peak intensity at 3463 cm^{-1}.

Figure 13. Difference FT-IR spectra of the adsorbed species on the surface of $nsGa_2O_3$(1123 K) (black line) and β-Ga_2O_3 (grey line) after the introduction of 45 Torr of CO_2.

Figure 14. UV-Vis diffuse reflectance spectra of $nsGa_2O_3$ and β-Ga_2O_3 (a) and those of Ag/$nsGa_2O_3$ and Ag/β-Ga_2O_3 after use for the photocatalytic CO_2 reduction test (b).

Figure 15. TEM images of Ag/$nsGa_2O_3$ (1123 K) (a, b) and Ag/β-Ga_2O_3 (c, d). Note the scale in (a) is different from the others.

Figure 16. The size distributions of the Ag nanoparticles on $nsGa_2O_3$ (1123 K) (a) and β-Ga_2O_3 (b).

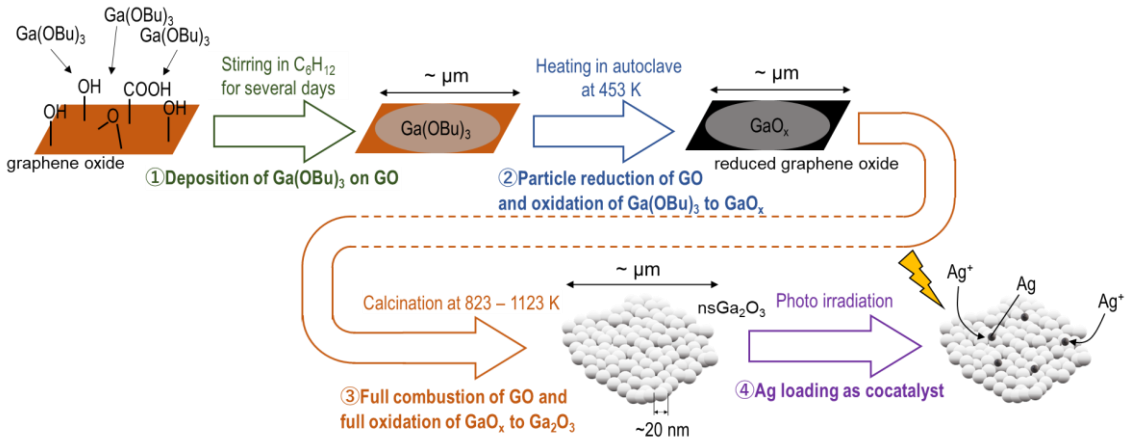

Figure 1. The schematic drawing for synthesis process of GaO_x/rGO, $nsGa_2O_3$, Ag/$nsGa_2O_3$.

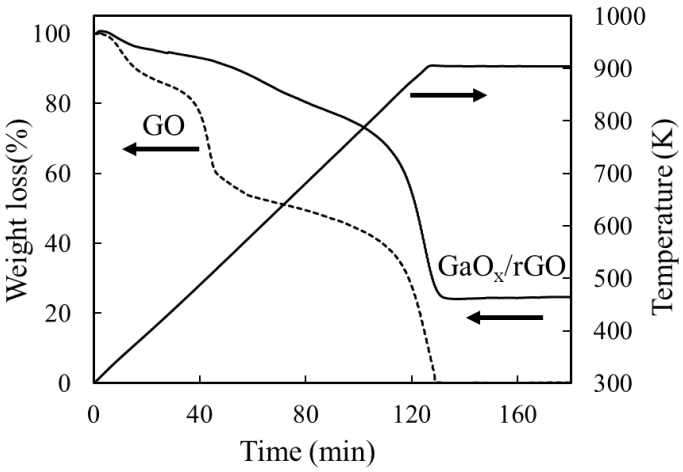

Figure 2. TGA profiles of GO and GaO_x/rGO measured in air.

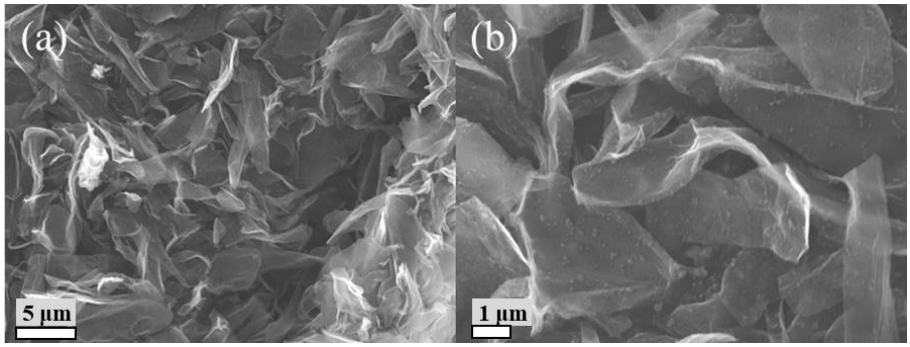

Figure 3. SEM image of GaO_x/rGO (a) with an enlarged view (b).

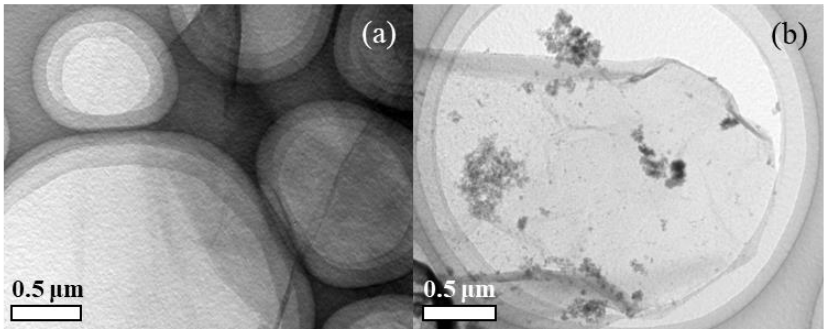

Figure 4. TEM images of GO (a), and GaO_x/rGO (b). Note that both are transparent or semi-transparent in TEM. Holes are owing to sample holder.

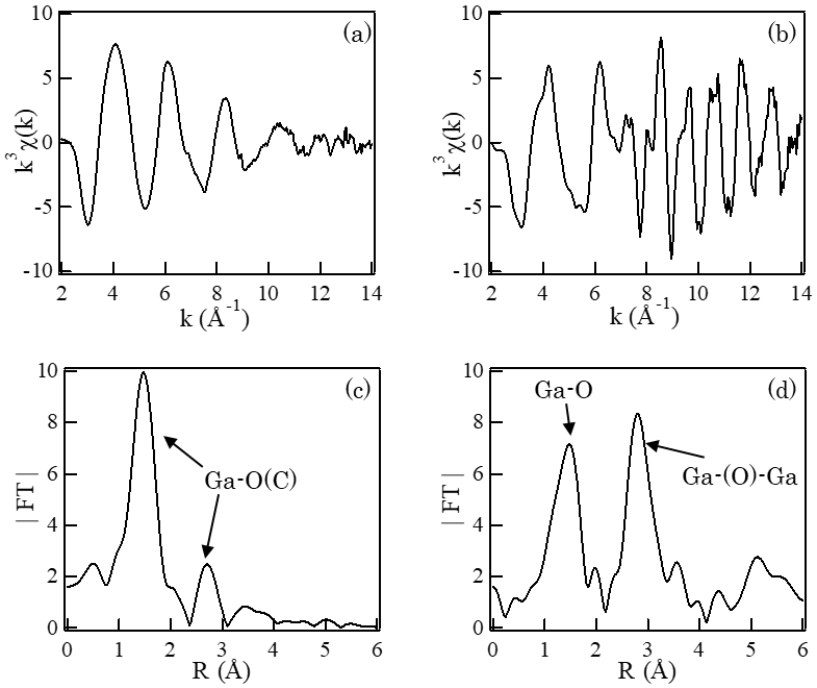

Figure 5. Ga K-edge EXAFS spectra of GaO_x/rGO (a) and β-Ga_2O_3 (b), and corresponding radial structure functions derived by Fourier transform of the EXAFS spectra of GaO_x/rGO (c) and β-Ga_2O_3 (d).

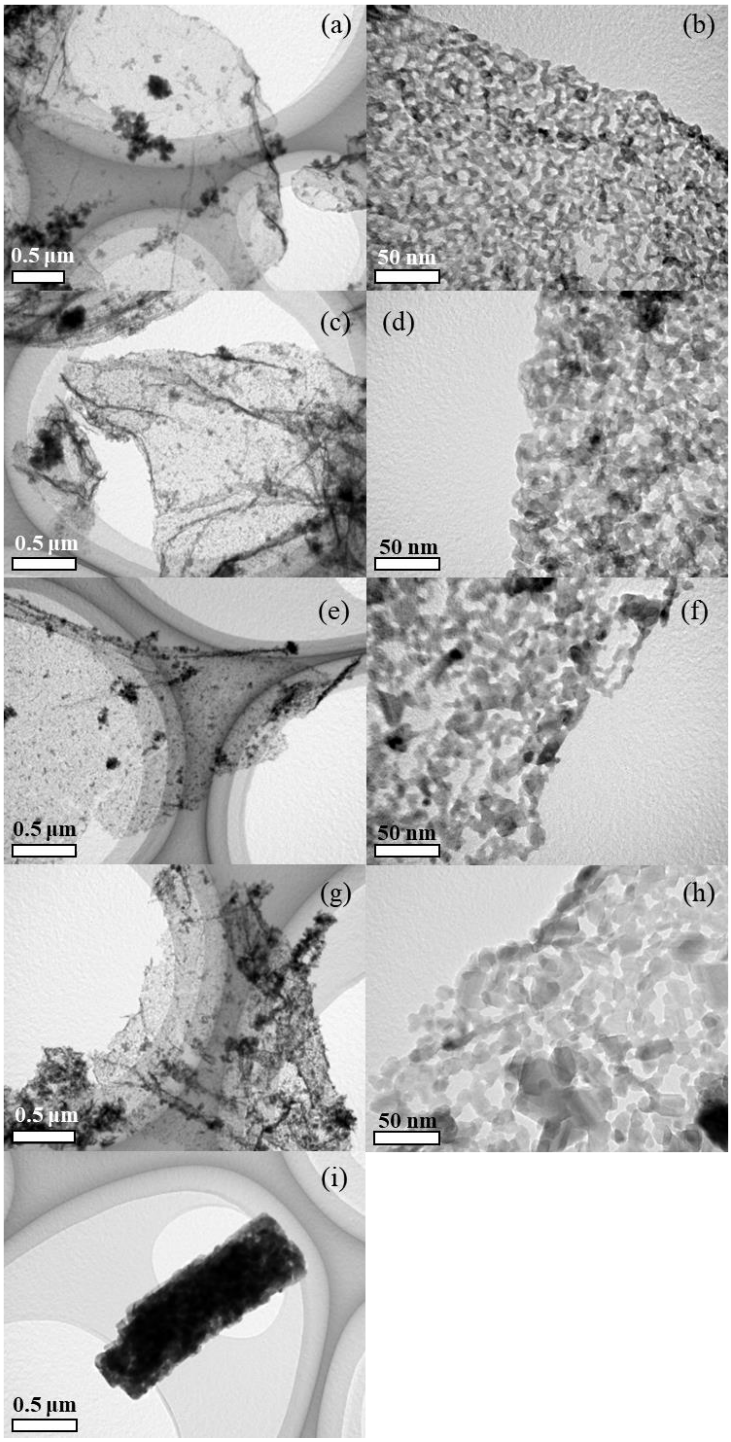

Figure 6. TEM images with different scales, for nsGa$_2$O$_3$(823 K) (a, b), nsGa$_2$O$_3$(923 K) (c, d), nsGa$_2$O$_3$(1023 K) (e, f), nsGa$_2$O$_3$(1123 K) (g, h) and β-Ga$_2$O$_3$ (i).

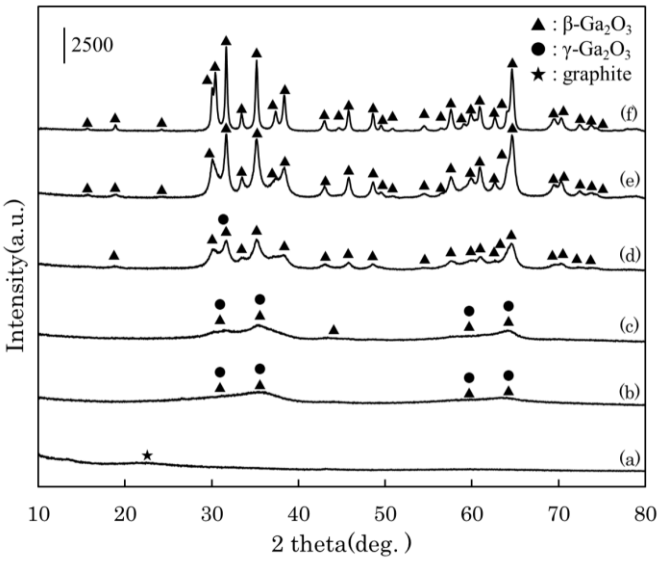

Figure 7. XRD patterns of GaO_x/rGO (a), nsGa_2O_3(823 K) (b), nsGa_2O_3(923 K) (c), nsGa_2O_3(1023 K) (d), nsGa_2O_3(1123 K) (e) and β-Ga_2O_3 (f).

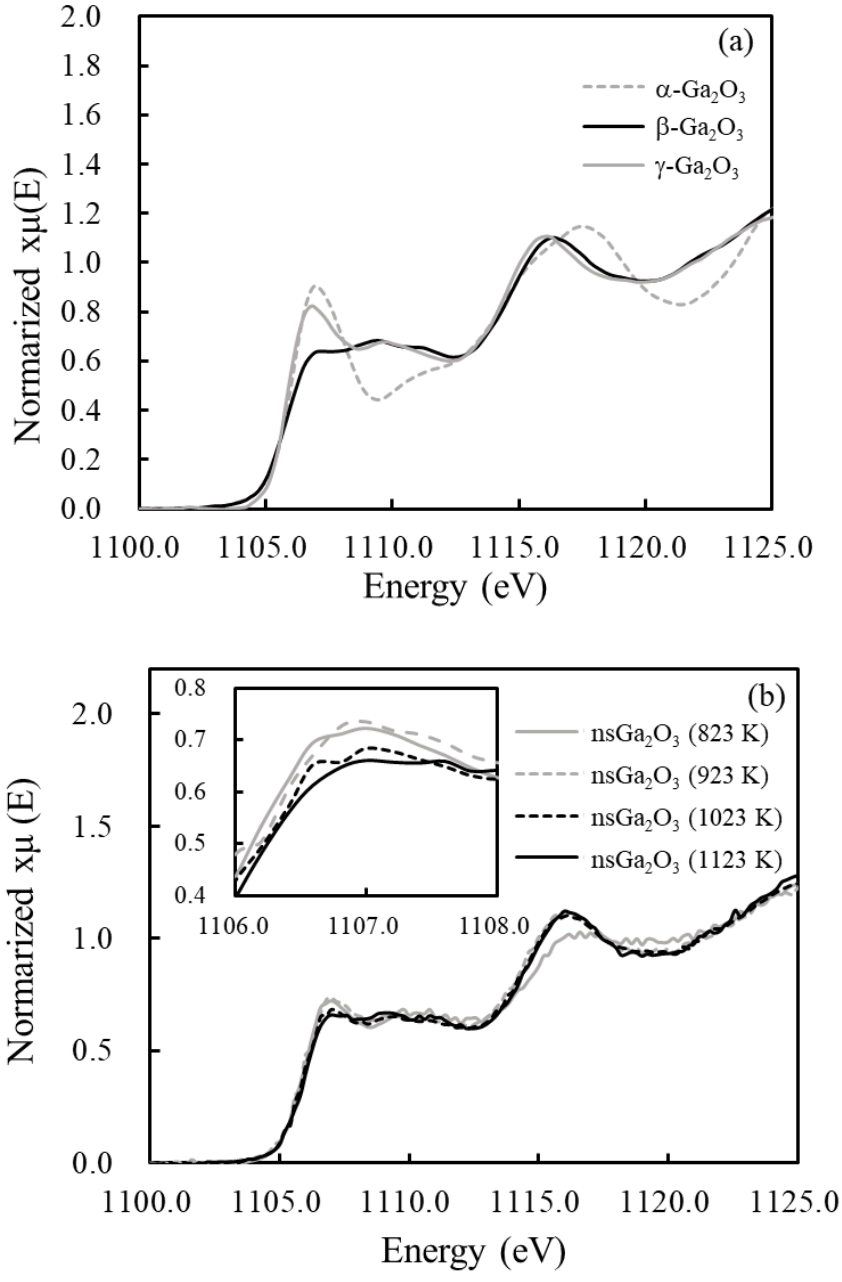

Figure 8. XANES spectra of α, β, γ-Ga_2O_3 as reference samples (a) and nsGa_2O_3 (823 – 1123 K) (b).

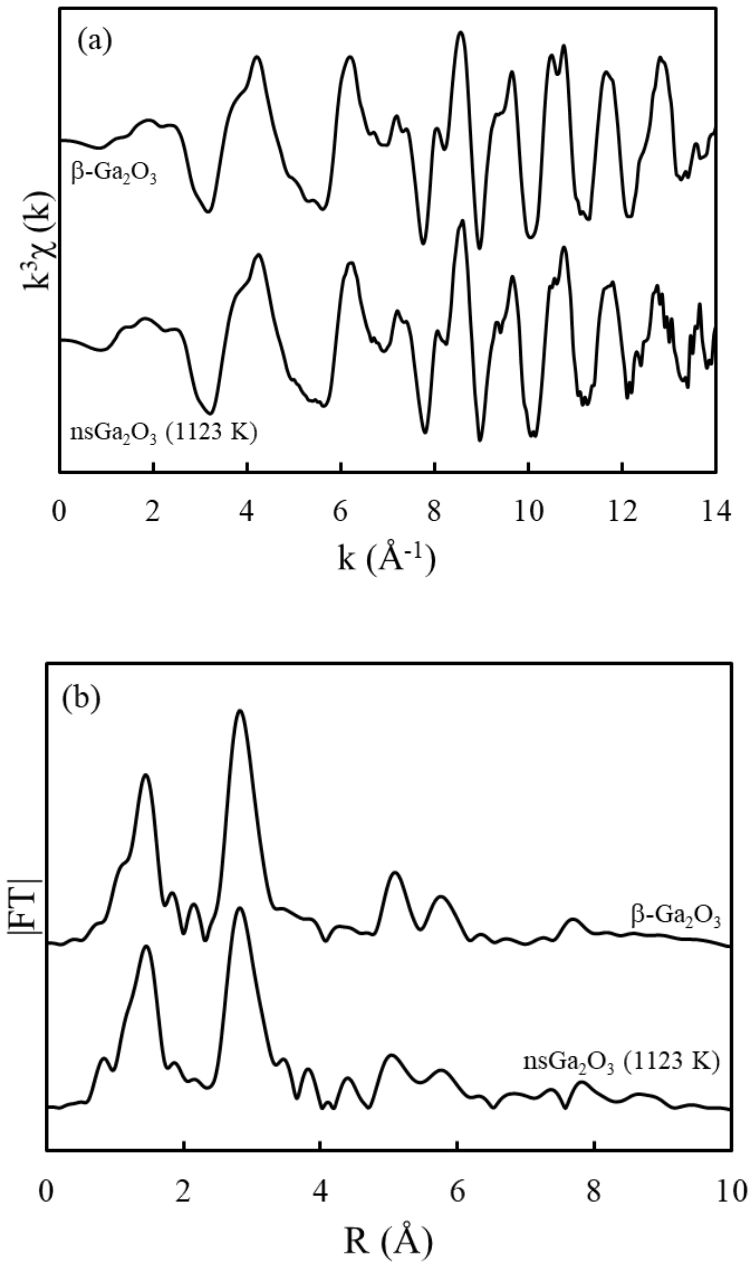

Figure 9. k^3-weighted Ga K-edge EXAFS spectra of $nsGa_2O_3$(1123 K) and β-Ga_2O_3 (a) and their radial structural functions obtained by Fourier transforming the EXAFS spectra (b).

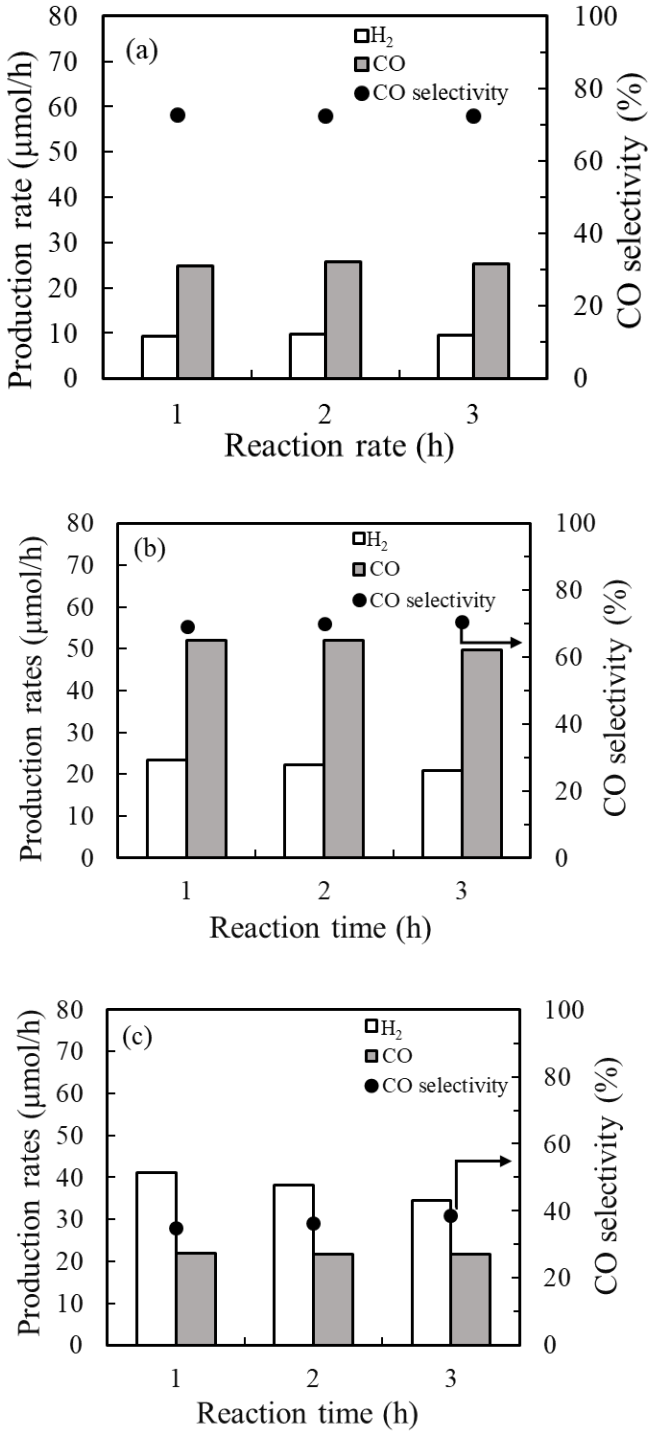

Figure 10. Comparison of H_2 and CO production rates and selectivity toward CO evolution between Ag/nsGa_2O_3(1023, 1123 K) (a, b) and Ag/β-Ga_2O_3 (c) in the photocatalytic CO_2 reduction.

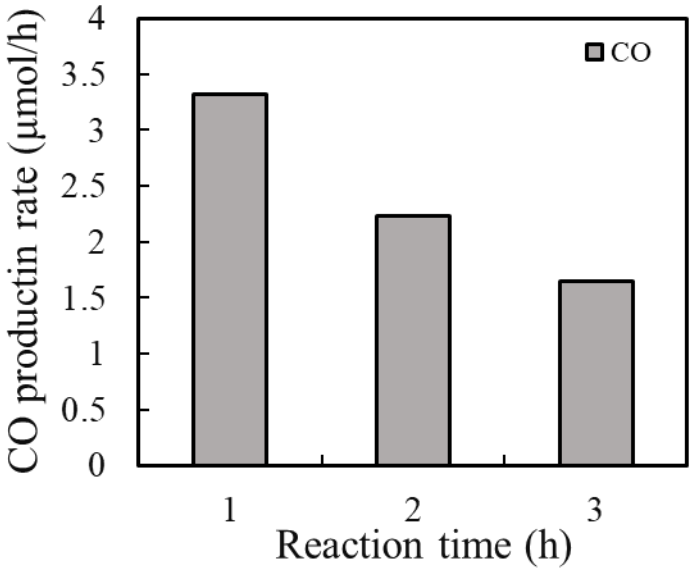

Figure 11. CO production rates in the photocatalytic reaction under He flow without CO_2 using nsGa_2O_3(1123 K).

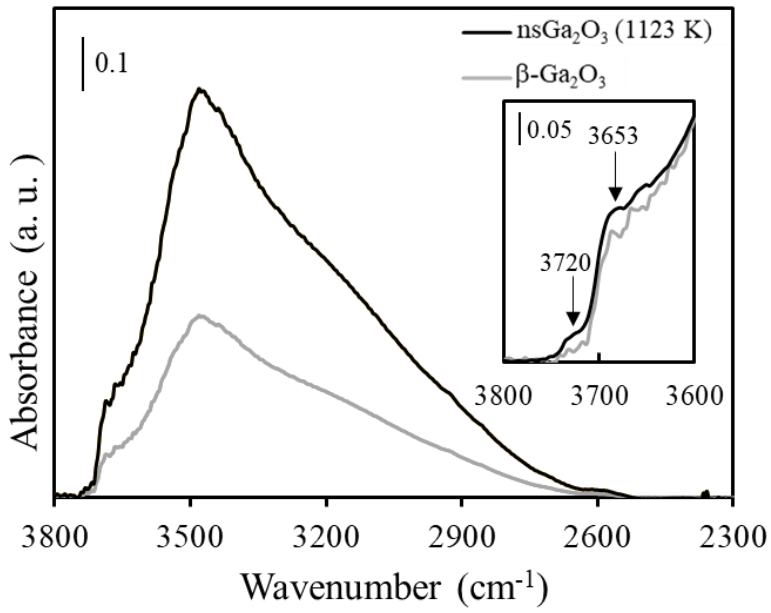

Figure 12. FT-IR spectra representing adsorbed water or hydroxyl groups on $nsGa_2O_3$(1123 K) (black line) and β-Ga_2O_3 (grey line). The inset shows normalized ones with the peak intensity at 3463 cm^{-1}.

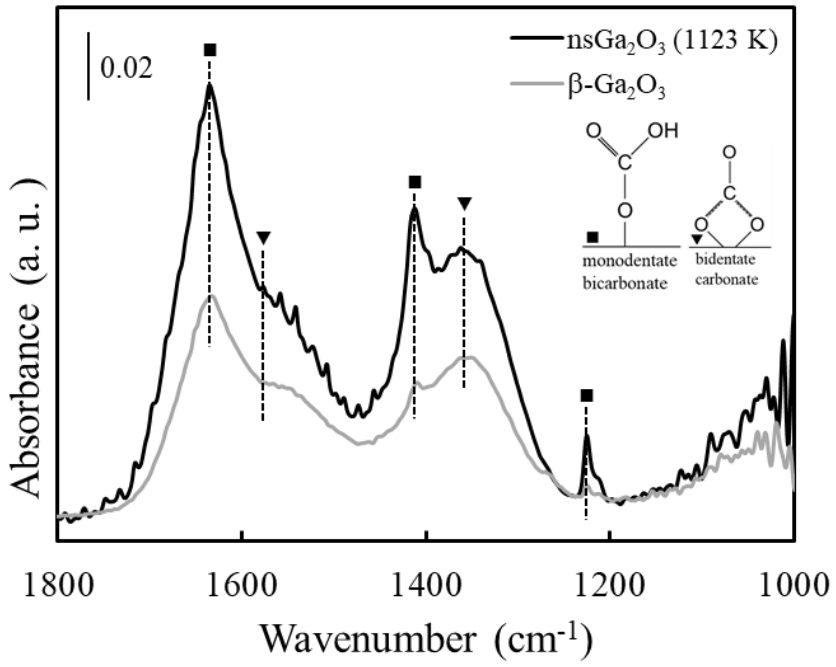

Figure 13. Difference FT-IR spectra of the adsorbed species on the surface of $nsGa_2O_3$(1123 K) (black line) and β-Ga_2O_3 (grey line) after the introduction of 45 Torr of CO_2.

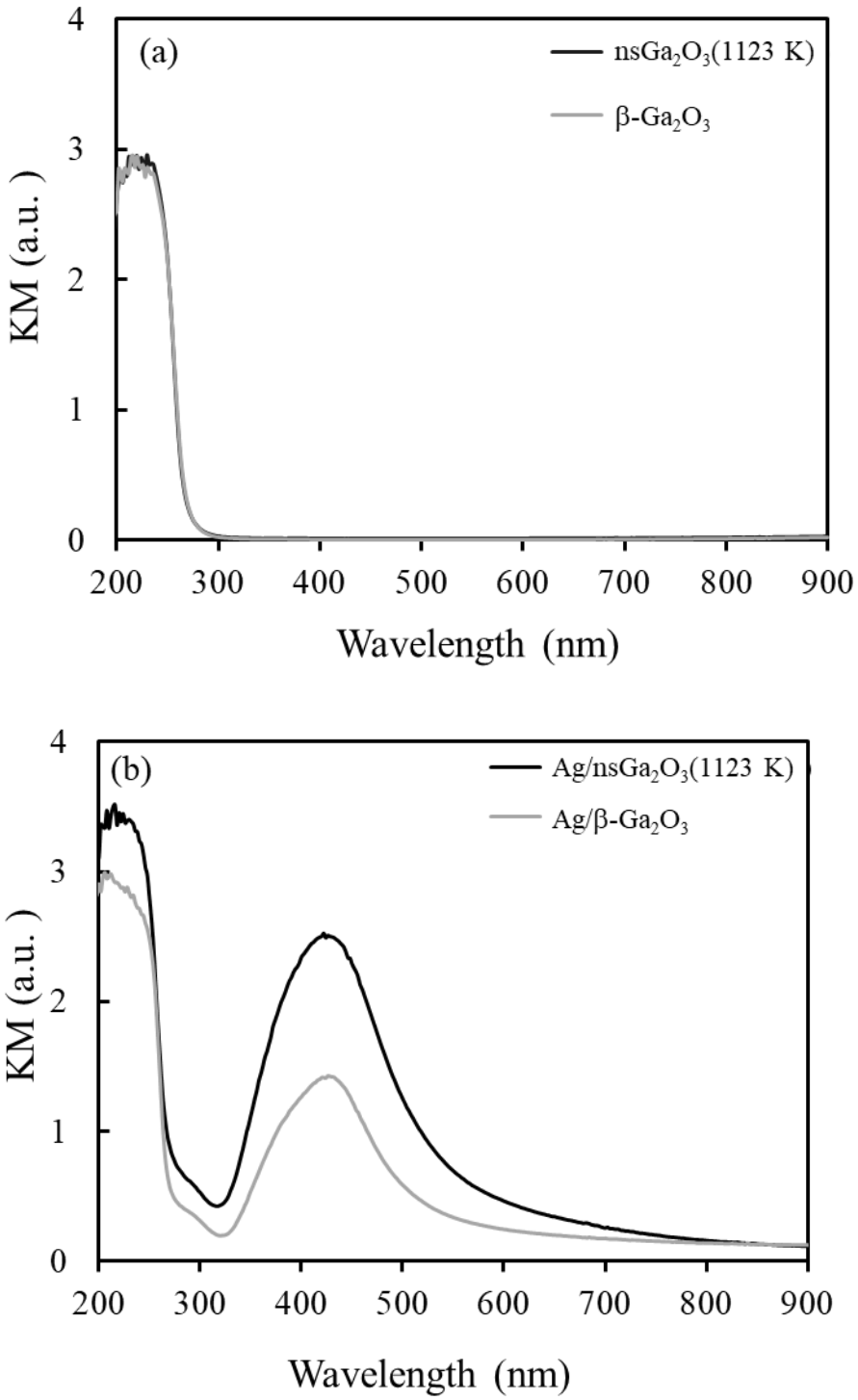

Figure 14. UV-Vis diffuse reflectance spectra of $nsGa_2O_3$ and β-Ga_2O_3 (a) and those of $Ag/nsGa_2O_3$ and Ag/β-Ga_2O_3 after use for the photocatalytic CO_2 reduction test (b).

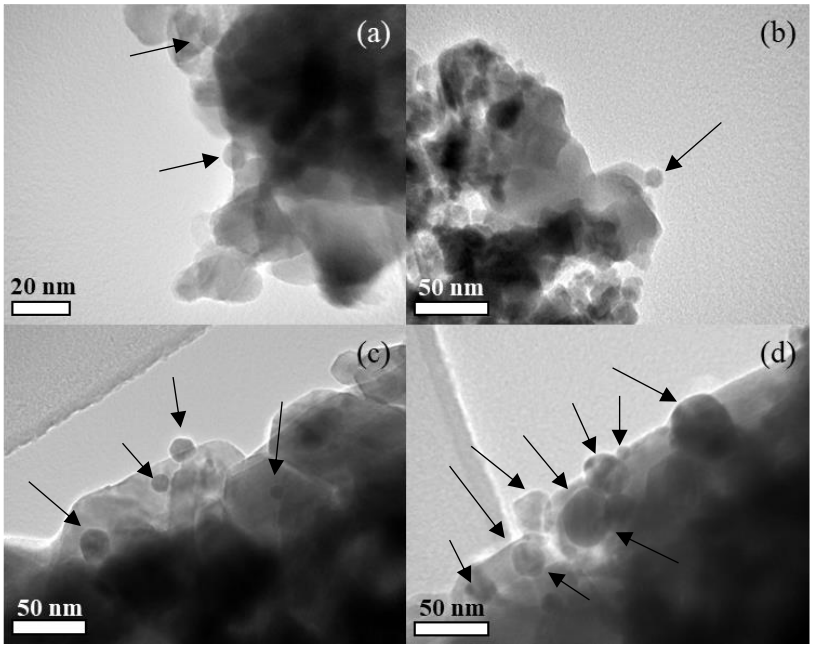

Figure 15. TEM images of Ag/nsGa_2O_3 (1123 K) (a, b) and Ag/β-Ga_2O_3 (c, d). Note the scale in (a) is different from the others.

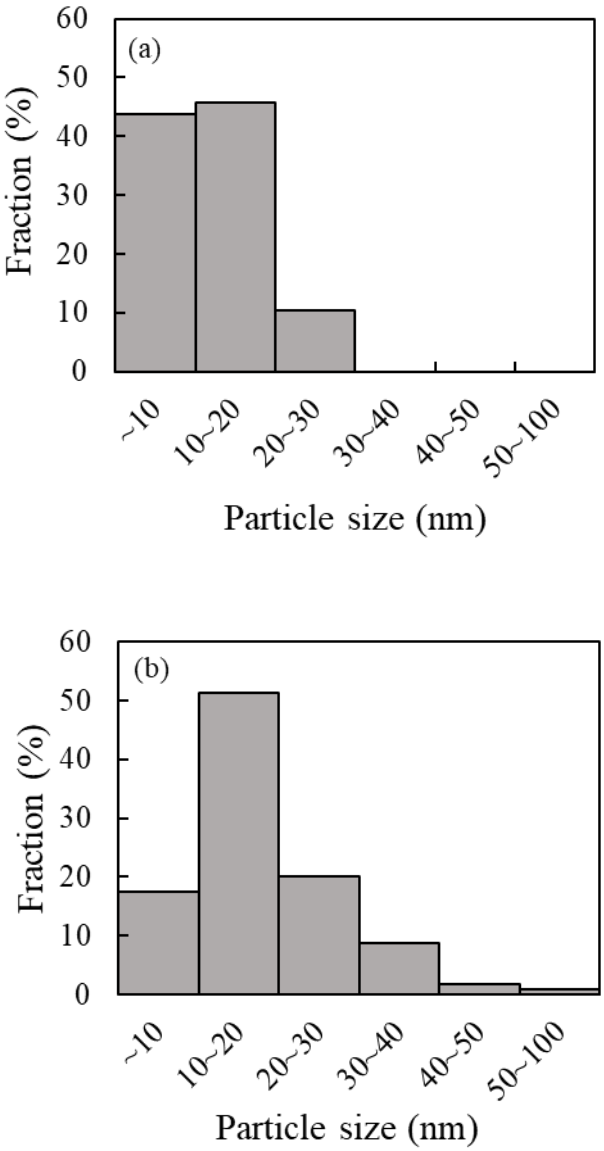

Figure 16. The size distributions of the Ag nanoparticles on nsGa_2O_3 (1123 K) (a) and β-Ga_2O_3 (b).